



HAL
open science

LOW FREQUENCY ELECTROMAGNETIC ENERGY HARVESTING FROM HIGHWAY BRIDGE VIBRATIONS

Michaël Peigney, Dominique Siegert

► **To cite this version:**

Michaël Peigney, Dominique Siegert. LOW FREQUENCY ELECTROMAGNETIC ENERGY HARVESTING FROM HIGHWAY BRIDGE VIBRATIONS. *Journal of Bridge Engineering*, 2020, 25 (8), pp.04020056. 10.1061/(ASCE)BE.1943-5592.0001581 . hal-03037866

HAL Id: hal-03037866

<https://enpc.hal.science/hal-03037866v1>

Submitted on 3 Dec 2020

HAL is a multi-disciplinary open access archive for the deposit and dissemination of scientific research documents, whether they are published or not. The documents may come from teaching and research institutions in France or abroad, or from public or private research centers.

L'archive ouverte pluridisciplinaire **HAL**, est destinée au dépôt et à la diffusion de documents scientifiques de niveau recherche, publiés ou non, émanant des établissements d'enseignement et de recherche français ou étrangers, des laboratoires publics ou privés.

LOW FREQUENCY ELECTROMAGNETIC ENERGY HARVESTING FROM HIGHWAY BRIDGE VIBRATIONS

Michaël Peigney¹ and Dominique Siegert²

ABSTRACT

This paper focuses on energy harvesting from low frequency vibrations in bridges via an electromagnetic device. Two pre-stressed concrete highway bridges are considered as case studies. In situ vibration measurements are reported and analyzed. An electromagnetic Vibration Energy Harvester (VEH) with a low resonant frequency (tunable around 4Hz) has been designed. That VEH is of the cantilever type, with 12 magnets mounted on a beam and acting as an inertial mass. By electromagnetic induction, the moving magnets produce an electric current in a surrounding conductive coil. A single degree-of-freedom model of the VEH is presented with the main purpose of estimating the electrical power generated under various operating conditions. A procedure for identifying the model parameters from simple measurements is described. Optimizing the coil geometry so as to maximize the electromechanical coupling is crucial to maximize the output power. That issue does not seem to have been addressed in the literature and is discussed in detail in this paper. The coil that has been fabricated approximates that optimal geometry. For harmonic excitation with normalized amplitude, the designed VEH achieves the best power density to date among experimentally validated low-frequency electromagnetic VEHs. During a field test on a highway bridge, the harvester produced an average power of 112 μW through a load resistance of 3.3 k Ω . We present a simple formula for estimating the output power of electromagnetic VEHs in terms of traffic intensity. That formula could be useful in future studies related to vibration energy harvesting in bridges.

Keywords: energy harvesting, electromagnetic transduction, bridge vibrations, field test.

INTRODUCTION

Energy harvesting has become a very active research topic in recent years (Priya and Inman 2009). The overall idea is to convert ambient energy into electrical energy that can be used as a complement or an alternative to batteries for powering wireless devices. Ambient energy may exist in several forms, such as thermal, electromagnetic or vibrational. Energy harvesting from vibrations, which is addressed in this paper, relies on a transduction mechanism for converting kinetic energy into electric energy. The most frequently used ones are the piezoelectric, the electromagnetic and the electrostatic transduction mechanisms (Stephen 2006).

This paper focuses on energy harvesting from vibrations in bridges. Vibration Energy Harvesters (VEHs) are usually designed as resonant systems. For a maximum efficiency, the resonance frequency is usually tuned to match the main frequency of the vibrations in the host structure. The design of VEHs usually targets small scale devices with resonant

¹Ph. D. Université Paris-Est, Laboratoire Navier (UMR 8205), CNRS, Ecole des Ponts ParisTech, IFSTTAR, F-77455 Marne la Vallée, France. Corresponding author, email: michael.peigney@polytechnique.org

²Ph. D. Université Paris-Est, IFSTTAR/COSYS, F-77455 Marne la Vallée, France.

38 frequencies above 30 Hz. Such high frequencies can be found in vibrations of machine tools,
39 which are characterized by peak accelerations in the range of 1–10 m s⁻² at frequencies
40 between 70 and 120 Hz (Reilly et al. 2011). In contrast, bridge vibrations are characterized
41 by low frequency (below 20 Hz) and small amplitude. Moreover, traffic-induced vibrations
42 are non periodic. In such conditions, energy harvesting is a challenging issue.

43 Both theoretical and experimental work has been devoted to vibration energy harvesting
44 in train bridges or highway bridges, mainly using piezoelectric materials (Ali et al. 2011;
45 Peigney and Siegert 2013; Cahill et al. 2018), electromagnetic induction (Galchev et al.
46 2011; Kwon et al. 2013; Caruso et al. 2016) or a combination of both (Toyabur et al. 2018;
47 Iqbal and Khan 2018). Although experimental investigations have been conducted, field tests
48 remain relatively rare. Kwon et al. (2013) designed an electromagnetic VEH with a resonant
49 frequency of 4.1 Hz and tested it on the 3rd Nongro bridge located in a rural area in South
50 Korea. An average power of 0.06 μ W was obtained over the 10-second period corresponding
51 to a heavy load truck crossing the bridge. The mean square acceleration measured on the
52 bridge was 0.144 m.s⁻². Peigney and Siegert (2013) designed a piezoelectric VEH and tested
53 it on a heavily trafficked highway bridge in France. That piezoelectric VEH was fixed on a
54 water pipe which was acting as an auxiliary vibrating structure with a resonant frequency
55 of 14.5 Hz. This paper aims at filling the gaps between existing field tests, by designing a
56 VEH with a low resonant frequency and testing it on a highway bridge. One objective is to
57 obtain representative values of the output power under real operating conditions.

58 Some vibration measurements carried out on 2 highway bridges are first reported. An
59 electromagnetic VEH with a low resonant frequency has been designed for testing on a
60 highway bridge. The designed VEH is of the cantilever type, with the magnets mounted on
61 a beam and acting as an inertial mass. By electromagnetic induction, the moving magnets
62 produce an electric current in a surrounding hand wound coil. A single degree-of-freedom
63 model of the electromagnetic VEH is introduced for estimating the mean electrical power.
64 In that model, the behavior of the VEH is captured by 5 parameters. The identification of
65 those parameters from simple measurements is detailed.

66 It is well known that the electromechanical coupling coefficient should be as large as
67 possible to maximize the efficiency of the VEH. Optimizing the coil geometry so as to max-
68 imize the electromechanical coupling is thus crucial. That issue does not seem to have been
69 addressed in the literature and is discussed in detail in this paper. The coil that has been
70 fabricated approximates that optimal geometry. Theoretical and experimental results on the
71 mean electrical power that can produced by the considered VEH are presented. Laboratory
72 tests are reported both for harmonic and non harmonic loadings. For harmonic loadings,
73 the average output power P_m is proportional to the mass M and to the square of the RMS
74 acceleration A_{rms} . The proposed device is shown to achieve the best P_m/MA_{rms}^2 ratio among
75 experimentally validated low-frequency VEHs reported in the literature. We believe this is
76 a consequence of the optimization of the electromechanical coupling.

77 Some results of a field test on a highway bridge are reported and compared with the-
78 oretical estimates. For designing VEHs fitted to bridge vibrations, it is desirable to have
79 an explicit formula for the output power. Such a formula is not readily available for elec-
80 tromagnetic VEHs under traffic-induced excitations. The difficulty is that traffic-induced
81 excitations are not harmonic in nature. By making use of the fact that traffic-induced exci-

tations are sequence of random short-time pulses, we derive an explicit formula for estimating the output power of electromagnetic VEHs in terms of traffic intensity. That formula could be useful in future studies related to vibration energy harvesting in bridges.

MEASUREMENTS OF TRAFFIC-INDUCED VIBRATIONS IN A BRIDGE

A very common type of bridges on heavily trafficked highways was chosen as a vibration source for energy harvesting. A first case study is the Roberval bridge located in the north of France (A1 highway) and shown in Fig. 1. The superstructure including the bridge deck is composed of five braced girder beams made of prestressed concrete. The span length is 33 m.

As traffic induced vibrations depend on complex truck-bridge interactions involving random loading characteristics, vibration data were collected on site in service conditions. Acceleration in the vertical direction was measured with a capacitive accelerometer located at mid-span of the outer girder. The accelerometer used is a GCDC X2-2 data logger set-up at the high sensitivity mode with a ± 1.25 g range and a 15-bit analog digital converter. The selected sample frequency was 128 Hz. Two hours of measurements were recorded during a time in the day when the traffic intensity was high (before midday). As the mean interarrival time between lorries crossing the bridge at high speed was about 12 s, the vibration response recorded lasted enough time for assuming stationarity of the random process involving weights of vehicles, arrival times, suspension systems of the vehicles and surface irregularities.

A typical record of the acceleration signal is shown in Fig. 2. The root mean square acceleration was $3.4 \cdot 10^{-2}$ m.s⁻². The related mechanical energy of vibration is mainly distributed among the first resonant frequencies of the bridge deck as shown in Fig. 3 where the mean power spectral density is displayed. The mean power spectral density of the measured acceleration was calculated with a frequency resolution of 0.02 Hz using the Welch's method implemented in Scilab, with 160 blocks of 5000 samples (Bunks et al. 2012). As can be observed in Fig. 3, two close resonant frequencies of the deck bridge are located at 4.1 Hz and 4.4 Hz in the spectrum. These frequencies are related to the first bending and torsion vibration modes of the superstructure (the terminology of the vibrations of a simply supported beam is adopted here). The resonant frequency at 14.5 Hz corresponds to the transverse bending mode. In Fig. 4 is shown the modal shape corresponding to the first bending mode, as obtained from a finite element calculation. The corresponding calculated frequency is 4 Hz. The frequencies provided by the finite element model for the next two relevant modes are 4.3 Hz and 15 Hz. Those values are relatively close to the experimental values (4.1, 4.4, 14.5 Hz). It can further be observed in Fig. 4 that the antinodes of the modes of vibration excited by the traffic are located at midspan of the outer girders beams.

As can be observed in Figs. 2 and 5(top), the acceleration signal is essentially a series of short-time pulses corresponding to lorries passing by. An example of an isolated pulse is shown in Fig. 6. Pulses are modulated periodic signals with an inner frequency about 4.1 Hz. The root mean square value of the peak acceleration of the pulses is about 0.11 m.s⁻².

A similar structure is also clearly observed on displacement measurements, see Fig. 5(bottom). The sample frequency was 100 Hz. In contrast with the acceleration signal, the pulses on the displacements are not modulated. Displacement measurements over a 2h30 period of time have been used to obtain statistics on the interarrival time between 2

consecutive pulses. The obtained histogram is shown in Fig. 7. In particular, the mean value of the interarrival time is 12.3 s.

Additional measurements were carried out on a similar highway bridge located in the south of France (Vareze bridge). For that bridge, the span length between the girder beams is 42 m. In Fig. 8 is shown a crossbraced girder beam of the Vareze bridge.

The mean power spectral density of the acceleration measured on the Vareze bridge is shown in Fig. 9. The root mean square acceleration was $3.6 \cdot 10^{-2} \text{ m}\cdot\text{s}^{-2}$, which is very close to the value obtained for the Roberval bridge. However, in contrast with the Roberval bridge, the power density is mainly concentrated at the first resonant frequency of the vibration modes of the bridge as can be observed in Fig. 9. It can also be observed that, as a result of the longer span length, the first resonant frequency (about 3 Hz) of the Vareze bridge is lower than that of the Roberval bridge.

DESIGN OF A RESONANT ELECTROMAGNETIC HARVESTER

A prototype cantilever-based electromagnetic harvester was designed for harvesting the low frequency traffic-induced vibrational energy of bridges. As low frequency and amplitude of movements were targeted, the proof mass of the inertial oscillator and the coil-permanent magnets arrangement were chosen for an effective electromechanical energy conversion. Although increasing the proof mass is beneficial for converting more mechanical energy into electrical energy, the experimental device had to be easily movable.

A global view of the device is shown in Fig 10. The main dimensions are indicated in Fig. 11. The two main components of the electromagnetic harvester are the magnetic circuit and the conductive coil, as shown in Figure 12. The magnetic circuit is composed of 12 permanent blocks magnets (neodymium grade N45). Each block magnet has dimensions $45 \times 30 \times 10 \text{ mm}$ and is magnetized through its width. The magnets are arranged on two ferromagnetic supports separated by an air gap of 8 mm. On each side of the air gap, the circuit hold two horizontal rows of 3 magnets with the same poling direction in the first row and opposite in the another one (Fig. 13). The poles of magnets facing through the air gap are the same, resulting in opposite magnetic fields in the upper and lower halves of the circuit. In Tables 1 and 2 are reported the locations and parameters of the magnets. The locations given in Table 1 are relative to an orthonormal frame with the x axis along the axis of the flat bar and the y axis along the bending direction. The magnetic circuit is supported by a cantilevered steel flat bar with cross section $2 \times 45 \text{ mm}^2$ and a length of 35 cm from the clamped end. The total mass of the magnetic circuit, the cantilever steel bar and the coil is 2.4 kg.

The conductive coil is made of an enameled copper wire (diameter 0.5 mm) wound on a rectangular PVC core (dimensions $120 \times 13 \text{ mm}$) resulting in an approximate ellipse shape with the dimensions in the principal axis equal to 150 and 55 mm. The width of the coil is 4 mm.

Note that an additional movable mass was set on the the flat bar for tuning the resonant frequency of the mechanical oscillations. The electrical load resistance R_L was connected to the coil so as to adjust the electromagnetic damping.

MODELLING

Single degree of freedom model

The single mode approximation for the vibrations of the energy harvester powering a resistive load R_L leads to the equation of a single degree of freedom harmonic oscillator with viscous damping

$$m\ddot{y} + (c_m + \frac{K^2}{R_L + r_i})\dot{y} + ky = ma \quad (1)$$

where m is the modal mass related to the displacement y at the center of the coil, k is the stiffness of the cantilever beam, c_m is the mechanical damping, r_i is the resistance of the coil and a is the acceleration of the inertial base excitation (Elvin and Elvin 2011). In (1), K is the electromechanical coupling coefficient, giving the electromotive force voltage V in the coil as

$$V = K\dot{y} \quad (2)$$

The power P in the electrical load is

$$P = \frac{R_L}{(R_L + r_i)^2} K^2 \dot{y}^2 \quad (3)$$

Consider an harmonic base excitation $a(t) = A \cos \omega t$. The steady state response can be written as $y(t) = \text{Re}(Y e^{i\omega t})$ where

$$Y = H(\omega)A$$

and

$$H(\omega) = \frac{m}{k - m\omega^2 + i\omega(c_m + \frac{K^2}{R_L + r_i})} \quad (4)$$

It follows that the average power \bar{P} in the electrical load is

$$\bar{P} = \frac{1}{2} \frac{R_L K^2}{(R_L + r_i)^2} |H(\omega)|^2 \omega^2 A^2$$

In particular, if the circular frequency ω of the excitation matches the natural circular frequency of the system $\omega_0 = \sqrt{k/m}$, the expression of the average power \bar{P} becomes

$$\bar{P} = \frac{1}{2} \frac{R_L}{((R_L + r_i)c_m + K^2)^2} K^2 m^2 A^2 \quad (5)$$

For later reference, we record the maximum value of \bar{P} in (5) that can be obtained from given parameters (K, r_i) . That value, henceforth denoted by $\bar{P}(K, r_i)$, is obtained by maximizing (5) with respect to the load resistance R_L . Solving the equation $\partial \bar{P} / \partial R_L = 0$ gives the optimal load

$$R_L^{opt} = r_i + \frac{K^2}{c_m} \quad (6)$$

The relation (6) can be interpreted as a relation of resistance matching in the electrical domain (Stephen 2006). The impedance optimization in more general situations has been studied by Cai and Zhu (2020). A practical energy harvesting circuit that can be treated as an equivalent resistor is presented by Cai and Zhu (2019).

Substituting (6) in (5) gives

$$\bar{P}(K, r_i) = \frac{K^2 m^2}{8c_m(c_m r_i + K^2)} A^2 \quad (7)$$

Identification of the model parameters

The model has 5 parameters, namely r_i , m , k , c_m , K . The resistance of the coil r_i was measured with a Fluke multimeter model 80 series 5 and was found to be equal to 8Ω . The other parameters were experimentally determined by measuring the displacement response in free vibration with a non-contact displacement transducer Micro-Epsilon NCDT 1302 and a digital acquisition card NI-9203. The mass distribution was first adjusted to tune the resonant frequency $\omega_0/2\pi$ to 4 Hz. The modal mass m was then derived from a small perturbation of the mass distribution by adding a mass $\Delta m = 78$ g at the center of the magnetic circuit for inducing a change $\Delta\omega_0$ in the resonant frequency. We have indeed the relation (Clough and Penzien 1975)

$$m = -\frac{1}{2} \frac{\Delta m}{\Delta\omega_0} \omega_0$$

That procedure yielded a modal mass m equal to 1.9 kg. The stiffness k was deduced from ω_0 and m through the relation $k = m\omega_0^2$.

The procedure used for measuring the electromechanical coupling coefficient K and the mechanical damping c_m from free vibrations is now detailed. First note that Eq. (1) can be rewritten as $m\ddot{y} + C\dot{y} + ky = ma$ where the effective damping

$$C = c_m + \frac{K^2}{R_L + r_i} \quad (8)$$

is the sum of the mechanical dissipation c_m and of the electrical dissipation by Joule's effect in the resistance $R_L + r_i$. For a fixed value of R_L , the parameter C can be estimated using measurements of the free decays. Repeating the procedure for several values of R_L leads to experimental points marked as crosses in Fig. 14. The experimental results display an affine dependence between C and $(R_L + r_i)^{-1}$, in accordance with (8). The values of K and c_m have been obtained by performing a linear regression on the experimental results shown in Fig. 14.

All the values of the parameters of the model of the energy harvester are reported in Table 3. For those parameters, the optimal load resistance as given by (6) is 4.2 k Ω .

DESIGN OPTIMIZATION OF THE COIL

This section addresses the theoretical issue of finding the coil geometry that maximizes the performance of the VEH. The coil that has been fabricated approximates the optimal geometry as will be discussed.

Expression of the electromechanical coupling coefficient

First consider a single conductive loop $\Gamma(t)$ moving in a time-independent magnetic field $\mathbf{B}(\mathbf{x})$. The magnetic flux $\Phi(t)$ in the loop is given by

$$\Phi(t) = \int_{\Sigma(t)} \mathbf{B}(\mathbf{x}) \cdot \mathbf{n} dS \quad (9)$$

where $\Sigma(t)$ is the surface closed by $\Gamma(t)$ and \mathbf{n} is the unit normal to $\Sigma(t)$. Assuming the loop to have a flat shape in the plane $(O, \mathbf{e}_x, \mathbf{e}_y)$ where $(O, \mathbf{e}_x, \mathbf{e}_y, \mathbf{e}_z)$ is an orthonormal frame, Eq. (9) becomes

$$\Phi(t) = \int_{\Sigma(t)} B_z(\mathbf{x}) dS \quad (10)$$

with $B_z = \mathbf{B} \cdot \mathbf{e}_z$.

The motion of the loop is described by a transformation $(x, y, t) \mapsto F(x, y, t)$ which gives the location at time t of a material point initially located at $(x, y, 0)$. Considering only small rigid body motions in the plane $(O, \mathbf{e}_x, \mathbf{e}_y)$, the transformation F can be written as

$$F(x, y, t) = (x - \theta(t)y + X(t), \theta(t)x + y + Y(t), 0) \quad (11)$$

where $(X(t), Y(t))$ corresponds to a translation motion and $\theta(t)$ is an angle of rotation. Using (11), expression (10) for the magnetic flux can be rewritten as

$$\Phi(t) = \int_{\Sigma(0)} B_z(F(x, y, t)) dS \quad (12)$$

Observing that the integration domain $\Sigma(0)$ is independent of time, we find

$$\frac{d\Phi(t)}{dt} = K_x \dot{X} + K_y \dot{Y} + K_\theta \dot{\theta} \quad (13)$$

with

$$\begin{aligned} K_x &= \int_{\Sigma(0)} \frac{\partial B_z}{\partial x}(x, y, 0) dS \\ K_y &= \int_{\Sigma(0)} \frac{\partial B_z}{\partial y}(x, y, 0) dS \\ K_\theta &= \int_{\Sigma(0)} -y \frac{\partial B_z}{\partial x}(x, y, 0) + x \frac{\partial B_z}{\partial y}(x, y, 0) dS \end{aligned} \quad (14)$$

In the following, we restrict our attention to loops that are *symmetric* with respect to the \mathbf{e}_x and the \mathbf{e}_y axis. We further assume that $B_z(x, -y, 0) = -B_z(x, y, 0) = -B_z(-x, y, 0)$ i.e. that the component B_z of the magnetic field (in the plane $(O, \mathbf{e}_x, \mathbf{e}_y)$) is *symmetric* with respect to the \mathbf{e}_x axis and *antisymmetric* with respect to the \mathbf{e}_y axis. In such case, it can easily be verified from expressions (14) that

$$K_x = K_\theta = 0$$

so that

$$\frac{d\Phi(t)}{dt} = K \dot{Y} \quad (15)$$

By Faraday's law of induction, the coefficient K identifies with the electromechanical coupling factor introduced in (2). Using (14) and Green's theorem, the coefficient K can be rewritten as

$$K = - \oint_{\Gamma(0)} B_z(x, y, 0) \mathbf{e}_x \cdot d\mathbf{l} \quad (16)$$

Shape optimization of the coil

In the following, attention is restricted to the situation where the magnetic field \mathbf{B} is created by a set of N identical block magnets, as in the designed prototype. All the magnets are assumed to have a uniform magnetization oriented along \mathbf{e}_z . The magnetization in magnet i is denoted by $\varepsilon_i M \mathbf{e}_z$ where M is a constant (independent of i). We have

$$B_z(x, y, 0) = \sum_{i=1}^N \varepsilon_i B_z^0(x - x_i, y - y_i, -z_i) \quad (17)$$

249 where (x_i, y_i, z_i) is the center of magnet i and B_z^0 denotes the z component of the magnetic
 250 field created by a reference cubic magnet centered at O and having a uniform magnetization
 251 $M\mathbf{e}_z$. The calculation of B_z^0 is a classical problem of magnetostatics (Jackson 1975; Smythe
 252 1988): We have

$$253 \quad B_z^0(x, y, z) = \frac{\mu_0 M}{4\pi} \sum_{\epsilon_1, \epsilon_2, \epsilon_3 \in \{-1, 1\}} \epsilon_1 \epsilon_2 \epsilon_3 \arctan \frac{(x - \epsilon_1 a_1)(y - \epsilon_2 a_2)}{(z - \epsilon_3 a_3)R} \quad (18)$$

where

$$R = \sqrt{(x - \epsilon_1 a_1)^2 + (y - \epsilon_2 a_2)^2 + (z - \epsilon_3 a_3)^2}$$

254 In (18), a_1 , a_2 and a_3 are half the length of the magnet in the \mathbf{e}_x , \mathbf{e}_y and \mathbf{e}_z directions,
 255 respectively. The constant μ_0 is the vacuum permeability ($\mu_0 = 4\pi \cdot 10^{-7}$ H/m).

256 The map of B_z in the plane $(0, \mathbf{e}_x, \mathbf{e}_y)$ is shown in Fig. 15 for a set of 12 N45 magnets
 257 with properties listed in Tables 1 and 2. As can be observed in Fig. 15, B_z is almost
 258 piecewise constant in the plane $(0, \mathbf{e}_x, \mathbf{e}_y)$. In more detail, $B_z(x, y, 0)$ is almost zero outside
 259 of rectangular domains (of dimensions $2a_1 \times 2a_2$) that are the projections of the magnets on
 260 the $(0, \mathbf{e}_x, \mathbf{e}_y)$ plane. In each of the 3 rectangular domains located in the half-plane $y \geq 0$,
 261 the magnetic field B_z is almost uniform and equal to

$$262 \quad B_0 = \frac{2\mu_0 M}{\pi} \sum_{\epsilon \in \{-1, 1\}} \epsilon \arctan \frac{a_1 a_2}{(z_1 - \epsilon a_3) \sqrt{(z_1 - \epsilon a_3)^2 + a_1^2 + a_2^2}} \quad (19)$$

263 The formula (19) gives $B_0 \simeq 0.5$ T. In each of the 3 rectangular domains located in the
 264 half-plane $y \leq 0$, the magnetic field B_z is almost uniform and equal to $-B_0$. Note that the
 265 special distribution of the magnetic field observed in Fig. 15 results from the fact that the
 266 distance between the magnets and the plane $(0, \mathbf{e}_x, \mathbf{e}_y)$ is small.

267 The observation that B_z is (almost) piecewise constant allows for great simplification in
 268 the shape optimization of the loop. Denoting by \mathcal{R} the set of rectangular domains in which
 269 B_z is non zero (Fig. 17), we have (as a first approximation)

$$270 \quad K = -B^0 \int_{\mathcal{R} \cap \Gamma(0)} \text{sgn}(y) \mathbf{e}_x \cdot d\mathbf{l} \quad (20)$$

271 Using the Cauchy-Schwarz inequality, Eq. (20) implies that

$$272 \quad K \leq 12B^0 a_1 \quad (21)$$

273 Eq. (21) is satisfied as an equality for any loop such that $\mathcal{R} \cap \Gamma(0)$ is parallel to the \mathbf{e}_x
 274 direction, as represented in Fig 16.

Consider now a planar coil (in the plane $(0, \mathbf{e}_x, \mathbf{e}_y)$) with N turns. Approximating each
 turn by a closed loop Γ_i , the flux $\Phi(t)$ in the coil satisfies the relation (15) with

$$K = -B^0 \sum_{i=1}^N \int_{\Gamma_i} \text{sgn}(y) \mathbf{e}_x \cdot d\mathbf{l}$$

275 It follows that

$$276 \quad K \leq 12B^0 N a_1. \quad (22)$$

277 Consider a coil such that (22) holds as an equality, i.e. such $\mathcal{R} \cap \Gamma_i$ is parallel to the \mathbf{e}_x
 278 direction, for all i . The maximum number N_{max} of turns in such a coil is $N_{max} = 2a_2/d$
 279 where d is the diameter of the wire. Hence the maximum value of K that can be achieved
 280 by a planar coil is

$$281 \quad K^{max} = 24 \frac{B^0}{d} a_1 a_2. \quad (23)$$

The formula (23) gives $K^{max} \simeq 8.1$ T.m. Among all the coils that satisfy $K = K^{max}$, the
 coil of minimal length as a rectangular shape as depicted in Fig 17. A simple calculation
 shows that the corresponding minimal length is

$$L \simeq \frac{2a_2}{d} (2a_2 + L_{\mathcal{R}})$$

282 where $L_{\mathcal{R}}$ is the length (in the \mathbf{e}_x direction) of the rectangle bounded by \mathcal{R} (see Fig. 17).
 283 For the data reported in Tables 1-2, we find $L \simeq 24$ m.

284 The formula (23) is approximate as it does not account for the variations of B_z at a fine
 285 length scale. For the rectangular coil shown in Fig. 17, a numerical calculation using the full
 286 expression (17) of the magnetic field gives $K \simeq 7.5$ T.m, which is about 10% smaller than
 287 the value obtained from (23).

288 Only planar coils have been considered so far, i.e. such that all the turns lie in the same
 289 plane. Larger values of K can be achieved by piling up turns in the \mathbf{e}_z direction, as depicted
 290 in Fig 18. Let e be the height (in the \mathbf{e}_z direction) of such a coil. In the optimal case of
 291 a compact packing (Fig. 18), the distance between 2 consecutive layers is $\sqrt{3}d/2$ and the
 292 number of layers M is approximatively $2e/(\sqrt{3}d)$. For a symmetric arrangement with respect
 293 to the plane $(0, \mathbf{e}_x, \mathbf{e}_y)$, the layer i is located in the plane $z = z_i$ with

$$294 \quad z_i = \frac{e - d}{2} \left(-1 + 2 \frac{i - 1}{M - 1} \right) \quad (24)$$

295 The coefficient K in such an arrangement can be written as

$$296 \quad K = \sum_{i=1}^M K^i \quad (25)$$

297 where K^i is the coefficient obtained for a planar coil lying in the plane $z = z_i$. For instance,
 298 consider a rectangular coil of height $e = 4$ mm in which each layer has the shape depicted in
 299 Fig 17. Combining (24) and (25) with the expression (17) of the magnetic field gives $K \simeq 68$
 300 T.m. That value takes into account the variation of the magnetic field in the z direction.
 301 The length of the wire in that coil is approximatively equal to 216 m.

302 **Approximation of the optimal coil**

303 The coil of the prototype tested was designed in such fashion as to approximate the
 304 optimal geometry in Fig. 17. A perfectly rectangular coil as shown in Fig. 17 is difficult
 305 to achieve in practice, notably because of bending stiffness effects. Consecutive turns tend
 306 to become progressively rounder. In the designed coil, the first inner turn Γ_1 is almost

307 rectangular with dimensions $2\tilde{a} \times 2\tilde{b}$ where $\tilde{a} = 120$ mm and $\tilde{b} = 6.5$ mm. The curve Γ_1 is
 308 thus defined by the equation

$$309 \quad \max\left(\left|\frac{x}{\tilde{a}}\right|, \left|\frac{y}{\tilde{b}}\right|\right) \leq 1 \quad (26)$$

310 The outer turn Γ_N is almost elliptical with semi-axes $a = 150$ mm and $b = 55$ mm. The
 311 curve Γ_N is thus defined by the equation

$$312 \quad \left\| \left(\frac{x}{a}, \frac{y}{b} \right) \right\|_2 = \sqrt{\left(\frac{x}{a} \right)^2 + \left(\frac{y}{b} \right)^2} \leq 1 \quad (27)$$

As i increases from 1 to N , the turn Γ_i gradually changes from a rectangular shape to an
 elliptical shape. To model the shape of Γ_i , consider the α -norm $\| \cdot \|_\alpha$ in \mathbb{R}^2 , defined for any
 $\alpha > 0$ by

$$\| (x, y) \|_\alpha = (|x|^\alpha + |y|^\alpha)^{1/\alpha}$$

313 A simple formula interpolating between (26) and (27) is

$$314 \quad \left\| \left(\frac{x}{a(\alpha)}, \frac{y}{b(\alpha)} \right) \right\|_\alpha \leq 1 \quad (28)$$

with

$$a(\alpha) = \tilde{a} + \frac{2}{\alpha}(a - \tilde{a}), \quad b(\alpha) = b + \frac{2}{\alpha}(b - \tilde{b})$$

315 Eq. (26) defining Γ_1 and Eq. (27) defining Γ_N can indeed be put in the form (28) with
 316 $\alpha \rightarrow \infty$ and $\alpha = 2$, respectively. Similarly, we model Γ_i by using Eq. (28) for some value
 317 of α (denoted by α_i) to be determined, as is now explained: Let $l(\alpha)$ be the length of the
 318 curve defined by (28) and $S(\alpha)$ be the area of the surface bounded by that curve. Setting
 319 $\alpha(1) = \infty$, the parameter α_i is found in a sequential fashion by use of the relation

$$320 \quad S(\alpha_{i+1}) = S(\alpha_i) + dl(\alpha_i) \quad (29)$$

321 where d is the diameter of the wire. The equation (29) is an approximate way of expressing
 322 the incompressibility of the wire. The coil geometry obtained from (29) is shown in Fig. 19
 323 for a wire diameter d of 0.5 mm. The planar coil shown in Fig. 19 has 32 turns and a length
 324 L of approximately 9.7 m.

325 The designed coil has a height of 4 mm. Assuming a compact packing has shown in
 326 Fig. 18, there are therefore 9 layers of wire in the e_z direction. Using the model geometry
 327 shown in Fig. 19 for each layer, the total length L and the coefficient K are found to be
 328 approximately equal to 87 m and 34 T.m respectively.

329 We note that the length L is related to the resistance r_i of the coil through the relation

$$330 \quad r_i = \frac{4\rho L}{\pi d^2} \quad (30)$$

331 Using the typical resistivity of copper ($\rho = 1.71 \cdot 10^{-8}$ Ω .m), the resistance r_i of the coil
 332 predicted by (30) is 7.6 Ω which is in good agreement with the value measured experimentally
 333 (equal to 8 Ω , see Table 3). The value $K = 34$ T.m obtained from the model geometry of
 334 the coil is also in relatively good agreement with the value measured experimentally from
 335 free vibrations (equal to 30 T.m, see Table 3). The discrepancy between the theoretical
 336 and experimental values of K can be partly attributed to the idealization of the geometry,
 337 notably regarding the assumption of compact packing.

RESULTS

Experimental tests and numerical simulations were carried out to get estimates of the mean electric power converted in the optimal load resistance of the designed electromagnetic harvester.

Laboratory test

The harvester was first tested with an electrodynamic shaker LDS V650 as shown in Fig. 20. The harvester was connected to a load resistance $R_L = 4.2 \text{ k}\Omega$. The shaker was driven by an amplified harmonic voltage delivered by a waveform generator Agilent 33250A. The frequency was set to 4.1 Hz in order to match the resonant frequency of the energy harvester. Such a low value was below the usable frequency range (5 Hz - 4 kHz) of the shaker, resulting in an acceleration signal that was not perfectly harmonic. The measured acceleration after band pass filtering is shown in Fig.21, its root mean square value was $A_{rms} = 0.02 \text{ m.s}^{-2}$. In contrast with the excitation signal, the output voltage was found to be harmonic with a constant amplitude (Fig. 22). This results from the resonant nature of the VEH which acts as a narrow band pass filter. The mean electrical power in the load resistance was $P_m = A_{rms}^2/R_L = 1.8 \text{ mW}$. Such a value is close to the theoretical value predicted by (7), which is equal to 1.7 mW for the excitation considered. This first test contributes to validate the model that has been presented previously.

The results for harmonic excitations can be used to compare the performance of the presented VEH with other devices from the literature. For an harmonic excitation, the average output power P_m is proportional to the mass M and to the square of the RMS acceleration A_{rms} . Experimental values of the ratio $P_m/M A_{rms}^2$ are reported in Table 4 for existing VEHs with low resonance frequency (below 5 Hz). The proposed device achieves a better $P_m/M A_{rms}^2$ ratio than existing low-frequency VEHs, which we believe is due to the optimization of the electromechanical coupling that has been carried out in the design of the presented VEH.

Field test

A test of the energy harvester was carried out on the bridge of Roberval. The device was set up at midspan of the outer girder beam. In Fig. 23 can be seen the energy harvester fixed on the superstructure as well as various equipments for measuring the bridge vibrations and the response of the energy harvester. In particular, the two dark green devices are GCDC X2-2 wireless accelerometers sensors, one being located at the clamped extremity of the cantilever (for measuring the base excitation) and the other being located on the VEH itself. Before installing the experimental device, the damping coefficient c_m was measured with the method of logarithmic decrement and found equal to 0.3 N.s.m^{-1} . The voltage measured at the output of the load resistance $R_L = 3.3 \text{ k}\Omega$ with a digital acquisition board NI USB6259 and is displayed in Fig. 24. The peak voltage was about 4 V. The experimental value of the mean electrical power was $112 \text{ }\mu\text{W}$. Those average values have been obtained over a testing time of approximately a 2 hours and a half around midday.

It is interesting to compare that value with that predicted by the model. The theoretical value of the mean harvester power P is obtained by calculating the average power on the time interval $[-T/2, T/2]$ and taking the limit $T \rightarrow +\infty$, i.e.

$$P = \lim_{T \rightarrow +\infty} \frac{1}{T} \int_{-T/2}^{T/2} \frac{R_L}{(R_L + r_i)^2} K^2 \dot{y}_T^2 dt \quad (31)$$

381 where $y_T(t)$ is the displacement of the coil for the gated acceleration signal a_T defined as
 382 $a_T(t) = a(t)$ if $|t| \leq T/2$, and $a_T(t) = 0$ otherwise. Parseval's theorem allows (31) to be
 383 rewritten as

$$384 \quad P = \lim_{T \rightarrow +\infty} \frac{1}{2\pi T} \int_{-\infty}^{\infty} \frac{R_L}{(R_L + r_i)^2} K^2 \omega^2 |\hat{y}_T(\omega)|^2 d\omega \quad (32)$$

where the superscript $\hat{\cdot}$ denotes the (non unitary) Fourier transform, e.g.

$$\hat{y}_T(\omega) = \int_{-\infty}^{+\infty} y_T(t) e^{-i\omega t} dt$$

385 Taking the Fourier transform of (1) shows that $\hat{y}_T(\omega) = H(\omega)\hat{a}_T(\omega)$ where $H(\omega)$ is defined
 386 as in (4). Hence (32) becomes

$$387 \quad \bar{P} = \frac{1}{2\pi} \frac{R_L K^2}{(R_L + r_i)^2} \int_{-\infty}^{+\infty} |H(\omega)|^2 S_a(\omega) \omega^2 d\omega \quad (33)$$

388 where

$$389 \quad S_a(\omega) = \lim_{T \rightarrow +\infty} \frac{|\hat{a}_T(\omega)|^2}{T} \quad (34)$$

390 is the power spectral density of the acceleration signal a as shown in Fig. 3. Eq. (33) yields
 391 a value of $97 \mu\text{W}$, which is in reasonable agreement with the measured value. As in the
 392 laboratory test, we can observe that the theoretical value underestimates the experimental
 393 value. The theoretical value for the optimal value of $4.2 \text{ k}\Omega$ for the load resistance is 104
 394 μW .

395 It is also interesting to compare the output power obtained with related results from field
 396 tests in the literature. In a previous study (Peigney and Siegert 2013), a piezoelectric energy
 397 harvester with a resonance frequency about 15 Hz was tested on the very same bridge. The
 398 mean electrical power generated was about $30 \mu\text{W}$, which is significantly less than what
 399 is obtained with the presented electromagnetic harvester. Interestingly, those two energy
 400 harvesters target different (and well-separated) resonance frequencies and therefore can work
 401 cooperatively. Comparing the efficiency of different VEHs can be performed by calculating
 402 power densities, defined as the ratio of the average output over the mass of the VEH. To be
 403 fair, such a comparison should be done for VEHs submitted to similar excitations. (Kwon
 404 et al. 2013) tested a 56g -heavy VEH on a bridge with a main resonant frequency of 4 Hz
 405 (as in our case). The average energy during a single burst excitation (corresponding to an
 406 individual lorry passing by) was measured to be about $6 \mu\text{W}$. The power density was thus
 407 about $105 \mu\text{W}/\text{kg}$. The VEH presented in this paper weighs about 2.14 kg . The average
 408 power over a single burst excitation can be obtained by dividing the power measured ($112 \mu\text{W}$)
 409 by the frequency of bursts ($1/12.3 \text{ Hz}$) and the duration of a pulse (here taken as 6 s), giving
 410 $213 \mu\text{W}$. The obtained power density is thus about $320 \mu\text{W}/\text{kg}$.

411 Additional predictions

412 Further investigations focus on extended predictions based on the model presented previ-
 413 ously and the recorded acceleration responses measured during in-situ testing. Experimental
 414 power spectral estimates of the vibrations measured on the Roberval and Vazeze bridges were
 415 used to this end.

416 In the case of Roberval bridge, the theoretical mean power estimate for the resonance at
 417 15 Hz is only 39 μW . This result was obtained keeping the same effective mass, damping
 418 and electromagnetic conversion parameters for the harvester. The resonance frequency of
 419 the harvester was tuned to 15 Hz by changing only its effective stiffness.

420 In the case of Vazeze bridge, the theoretical mean power estimate for the resonance at
 421 3 Hz is about 500 μW . That value is again obtained by changing only the effective stiffness
 422 so as to tune the resonant frequency of the harvester to 3 Hz. The relatively high value
 423 obtained from the Vazeze bridge stems from the fact that the vibration energy in the bridge
 424 is concentrated on a single peak (Fig. 9) instead of two close but distinct peaks as in the
 425 case of the Roberval bridge (Fig. 3).

426 Those results have been obtained under perfect tuning conditions: the resonance fre-
 427 quency of the harvester matches the targeted resonance frequency of the bridge. In real
 428 world applications, detuning effects are expected to come at play and need to be considered
 429 in the analysis. Even if perfectly tuned initially, the harvester may indeed detune due to
 430 external conditions. A related and perhaps more critical effect is the variation of the reso-
 431 nance frequencies of the bridge with the ambient temperature. The resonance frequencies of
 432 the bridge indeed decrease with the temperature. In a first approximation, that dependence
 433 is linear with a slope of 0.02 Hz per $^{\circ}\text{C}$ (Siegert et al. 2009). To put things in perspective,
 434 meteorological data collected over recent years show (MeteoFrance 2019) that the average
 435 monthly temperature on the bridge location vary between 4.2 $^{\circ}\text{C}$ and 18.5 $^{\circ}\text{C}$. This corre-
 436 sponds approximatively to a 0.3 Hz variation of the resonant frequency (around 4.Hz).

437 In order to study the influence of detuning on the performance of the harvester, the
 438 mean electrical power was calculated for different values of the resonant frequency of the
 439 harvester (around 4 Hz). The results are shown in Fig. 25. The acceleration time record of
 440 the response of the Roberval bridge has been used in those calculations. As can observed in
 441 Fig. 25, the harvested electrical power is less than 50% of the maximum estimate when the
 442 tuning frequency is lower than 3.9 Hz or higher than 4.4 Hz.

443 A similar analysis has been done for the Vazeze bridge. The corresponding results are
 444 shown in Fig. 26. For the Vazeze bridge, the half power bandwidth is about 0.2 Hz and
 445 hence much smaller than in the case of the Roberval bridge. However, even for a relatively
 446 large detuning (± 0.25 Hz), the output power predicted for the Vazeze bridge remains larger
 447 than the maximum output power obtained for the Roberval bridge.

448 **A simple formula for estimating the harvested power**

449 As observed previously, traffic-induced excitations are essentially sequences of short-time
 450 pulses corresponding to individual lorries passing by. In a first approximation, each pulse
 451 is a modulated periodic signal with an inner circular frequency ω_i related to the modal
 452 frequencies of the bridge and the location of the harvester. Those observations can be used
 453 to obtain a simple model for relating the mean harvested power to traffic statistics. To this
 454 end, a pulse is here approximated by a function of the form

$$455 \quad A f_0(t) \tag{35}$$

456 where

$$457 \quad f_0(t) = \text{tri}(t) \cos \omega_i t \tag{36}$$

458 and $\text{tri}(t)$ is the triangle function defined as

$$459 \quad \text{tri}(t) = \begin{cases} 0 & \text{for } |t| > M \\ 1 + t/M & \text{for } -M \leq t \leq 0 \\ 1 - t/M & \text{for } 0 \leq t \leq M \end{cases} \quad (37)$$

460 The function f_0 is represented in Figure 27. In (35), the parameter M characterizes the
461 duration of the pulse and A is the peak level. Consider a nonperiodic train of pulses

$$462 \quad a(t) = \sum_{k=-\infty}^{+\infty} A_k f_0(t - t_k) \quad (38)$$

463 where A_k and t_k are random variables. Using brackets $\langle \rangle$ to denote ensemble averages, we
464 obtain from (33) that

$$465 \quad \langle \bar{P} \rangle = \frac{1}{2\pi} \int_{-\infty}^{\infty} \frac{R_L}{(R_L + r_i)^2} K^2 \omega^2 S_a(\omega) |H(\omega)|^2 d\omega \quad (39)$$

466 where $S_a(\omega)$ is now defined by

$$467 \quad S_a(\omega) = \lim_{T \rightarrow +\infty} \frac{\langle |\hat{a}_T(\omega)|^2 \rangle}{T} \quad (40)$$

468 We refer to the textbooks of Drake (1967) and Mix (1995) for more details on random signal
469 theory. Assuming that pulse emission events are independent, the spectral density S_a of a
470 random train of pulses (38) can be calculated using Carson's theorem (Carson 1931; Mix
471 1995), giving

$$472 \quad S_a(\omega) = N \langle A^2 \rangle |\hat{f}_0(\omega)|^2 + 2\pi \delta(\omega) \left[N \langle A \rangle \int_{-\infty}^{+\infty} f_0(t) dt \right]^2 \quad (41)$$

473 where N is the average rate of pulse emission and δ is the Dirac distribution. Substituting
474 (41) in (39) yields

$$475 \quad \langle \bar{P} \rangle = N \langle A^2 \rangle E_0 \quad (42)$$

476 where

$$477 \quad E_0 = \frac{1}{2\pi} \frac{R_L}{(R_L + r_i)^2} K^2 \int_{-\infty}^{+\infty} |\hat{f}_0(\omega)|^2 |H(\omega)|^2 \omega^2 d\omega \quad (43)$$

It can be calculated from (36) that

$$|\hat{f}_0(\omega)|^2 = \frac{M^2}{4} \left(\text{sinc}^2 \frac{M(\omega_i + \omega)}{2} + \text{sinc}^2 \frac{M(\omega_i - \omega)}{2} \right)^2$$

478 Using the model parameters reported in (3) and taking $\omega_i/2\pi = 4.1$ Hz, $c_m = 0.3$ N.m.s⁻¹,
479 $R_L = 3.3$ k Ω , the energy E_0 in (43) is equal to 0.106 J. As reported previously, the root mean
480 square value $\sqrt{\langle A^2 \rangle}$ of the peak acceleration is 0.11 m.s⁻² for the Roberval bridge. The
481 mean value of the interarrival time between two pulses is 12.3 s, hence the average rate of
482 pulse emission N is equal to 1/12.3 Hz. Using those values, formula (42) yields $\langle \bar{P} \rangle = 105$
483 μ W, which is quite close to the measured value (112 μ W). Eq. (42) is approximate but is of
484 very simple use. It allows one to estimate the harvested energy in terms of traffic intensity.

CONCLUSION

The designed electromagnetic VEH targets the first bending and vibration modes of the highway bridges considered. The corresponding frequency are about 4Hz and the root mean square acceleration is about $3.5 \cdot 10^{-2} \text{ m.s}^{-2}$. The chosen coil geometry as be chosen in such fashion to optimize the electromechanical coupling. During field test, the electrical power generated by the VEH was $112 \mu\text{W}$ with a peak voltage of 4 V. That average power was obtained over approximatively 2 h 30 min of field testing. A single degree-of-freedom model with 5 parameters has been presented. That model allows to get approximate but simple estimates of the output power under various operating conditions. In particular, values up to $500 \mu\text{W}$ are expected to be obtained on the Varese bridge for which the vibration energy is concentrated on a single peak.

In the context of structural health monitoring, the harvested energy could be used to power wireless sensor nodes. To put things in perspective, it has been shown in (Reilly et al. 2011) that a wireless acceleration sensor transmitting every 10 seconds requires a power of 3 mW. Cross multiplication suggests that the power generated by the presented VEH on the Roberval bridge ($112 \mu\text{W}$) could be used for feeding a wireless sensor transmitting every 5 minutes or so, which could be relevant for slow time varying quantities such as temperature, humidity or air pollution.

It would be interesting to go further in that direction by combining the designed electromagnetic VEH with a power conditioning circuit and a dedicated sensor with low duty cycle. Future work will focus on improving the performance of the device. In that regard, other pole arrangements could be considered. For electromagnetic dampers, it was indeed found that the energy density could be improved by considering several rows of magnets with alternated poles (Zuo et al. 2011). In this paper, we used two rows of magnets but considering additional rows would possibly be helpful in improving the electromechanical coupling. The shape and arrangements of the coils should be optimized accordingly. Another possible strategy for improving the performance of the device is to make use of nonlinear phenomena such a bistability (Harne and Wang 2013), impact (Cottone et al. 2014) or parametric resonance (Mam et al. 2017).

DATA AVAILABILITY

Data, models, and Matlab code generated during the study are available from the corresponding author by request.

ACKNOWLEDGEMENTS

The authors thank Roland Vidal (SNCF), Amer Abouzeid (Sixense), Xavier Chapeleau (IFSTTAR) and Erick Merliot (IFSTTAR) for their help.

APPENDIX I. REFERENCES

- 520
521 Ali, S., Friswell, M., and Adhikari, S. (2011). “Analysis of energy harvesters for highway
522 bridges.” *Journal of Intelligent Material Systems and Structures*, 22(16), 1929–1938.
- 523 Bunks, C., Chancelier, J.-P., Delebecque, F., Goursat, M., Nikoukhah, R., and Steer, S.
524 (2012). *Engineering and scientific computing with Scilab*. Springer Science & Business
525 Media.
- 526 Cahill, P., Mathewson, A., and Pakrashi, V. (2018). “Experimental validation of piezo-
527 electric energy-harvesting device for built infrastructure applications.” *Journal of Bridge
528 Engineering*, 23(8), 04018056.
- 529 Cai, Q. and Zhu, S. (2019). “Enhancing the performance of electromagnetic damper cum
530 energy harvester using microcontroller: Concept and experiment validation.” *Mechanical
531 Systems and Signal Processing*, 134, 106339.
- 532 Cai, Q. and Zhu, S. (2020). “Unified strategy for overall impedance optimization in vibration-
533 based electromagnetic energy harvesters.” *International Journal of Mechanical Sciences*,
534 165, 105198.
- 535 Carson, J. R. (1931). “The statistical energy-frequency spectrum of random disturbances.”
536 *Bell System Technical Journal*, 10(3), 374–381.
- 537 Caruso, G., Chirianni, G., and Vairo, G. (2016). “Energy harvesting from wind-induced
538 bridge vibrations via electromagnetic transduction.” *Engineering Structures*, 115, 118–
539 128.
- 540 Clough, R. W. and Penzien, J. (1975). “Structural dynamics.” *McGrawHill Inc, New York
541 zbMATH*.
- 542 Cottone, F., Frizzell, R., Goyal, S., Kelly, G., and Punch, J. (2014). “Enhanced vibrational
543 energy harvester based on velocity amplification.” *Journal of Intelligent Material Systems
544 and Structures*, 25(4), 443–451.
- 545 Drake, A. W. (1967). *Fundamentals of applied probability theory*. Mac Graw Hill.
- 546 Elvin, N. G. and Elvin, A. A. (2011). “An experimentally validated electromagnetic energy
547 harvester.” *Journal of Sound and Vibration*, 330(10), 2314–2324.
- 548 Galchev, T., McCullagh, J., Peterson, R., and Najafi, K. (2011). “Harvesting traffic-induced
549 vibrations for structural health monitoring of bridges.” *Journal of Micromechanics and
550 Microengineering*, 21(10), 104005.
- 551 Harne, R. and Wang, K. (2013). “A review of the recent research on vibration energy har-
552 vesting via bistable systems.” *Smart materials and structures*, 22(2), 023001.
- 553 Iqbal, M. and Khan, F. U. (2018). “Hybrid vibration and wind energy harvesting using
554 combined piezoelectric and electromagnetic conversion for bridge health monitoring appli-
555 cations.” *Energy Conversion and Management*, 172, 611–618.
- 556 Jackson, J. D. (1975). *Classical electrodynamics*. John Wiley & Sons.
- 557 Jung, H.-J., Kim, I.-H., and Jang, S.-J. (2011). “An energy harvesting system using the wind-
558 induced vibration of a stay cable for powering a wireless sensor node.” *Smart materials
559 and structures*, 20, 075001.
- 560 Kwon, S.-D., Park, J., and Law, K. (2013). “Electromagnetic energy harvester with re-
561 pulsively stacked multilayer magnets for low frequency vibrations.” *Smart materials and
562 structures*, 22(5), 055007.
- 563 Mam, K., Peigney, M., and Siegert, D. (2017). “Finite strain effects in piezoelectric energy

564 harvesters under direct and parametric excitations.” *Journal of Sound and Vibration*, 389,
565 411–437.

566 MeteoFrance (2019). “Public data, <<https://donneespubliques.meteofrance.fr>>.

567 Mix, D. F. (1995). *Random signal processing*. Prentice-Hall, Inc.

568 Peigney, M. and Siegert, D. (2013). “Piezoelectric energy harvesting from traffic-induced
569 bridge vibrations.” *Smart Materials and Structures*, 22(9), 095019.

570 Priya, S. and Inman, D. J. (2009). *Energy harvesting technologies*, Vol. 21. Springer.

571 Reilly, E. K., Burghardt, F., Fain, R., and Wright, P. (2011). “Powering a wireless sensor node
572 with a vibration-driven piezoelectric energy harvester.” *Smart materials and structures*,
573 20(12), 125006.

574 Siegert, D., Mevel, L., Reynders, E., De Roeck, G., and Goursat, M. (2009). “Variation of
575 modal parameter estimates of a prestressed concrete bridge.” *27th International Modal
576 Analysis Conference (IMAC-XXVII)*.

577 Smythe, W. B. (1988). *Static and dynamic electricity*. Hemisphere publishing.

578 Stephen, N. G. (2006). “On energy harvesting from ambient vibration.” *Journal of sound
579 and vibration*, 293(1-2), 409–425.

580 Toyabur, R., Salauddin, M., Cho, H., and Park, J. Y. (2018). “A multimodal hybrid energy
581 harvester based on piezoelectric-electromagnetic mechanisms for low-frequency ambient
582 vibrations.” *Energy Conversion and Management*, 168, 454–466.

583 Zuo, L., Chen, X., and Nayfeh, S. (2011). “Design and analysis of a new type of electromag-
584 netic damper with increased energy density.” *Journal of vibration and acoustics*, 133(4),
585 041006.

TABLE 1. Locations and orientations of the magnets

i	x_i (mm)	y_i (mm)	z_i (mm)	ϵ_i
1	-47.5	17.5	9	-1
2	0	17.5	9	-1
3	47.5	17.5	9	-1
4	-47.5	-17.5	9	1
5	0	-17.5	9	1
6	47.5	-17.5	9	1
7	-47.5	17.5	-9	-1
8	0	17.5	-9	-1
9	47.5	17.5	-9	-1
10	-47.5	-17.5	-9	1
11	0	-17.5	-9	1
12	47.5	-17.5	-9	1

TABLE 2. Parameters of the magnets

a_1 (mm)	a_2 (mm)	a_3 (mm)	$\mu_0 M$ (T)
22.5	15	5	1.32

TABLE 3. Estimated values of the parameters of the electromagnetic harvester.

m (kg)	k (N·m ⁻¹)	c_m (N·s·m ⁻¹)	K (T·m)	r_i (Ω)
1.9	1260	0.22	30.3	8

TABLE 4. Experimental results for harmonic excitations on low-frequency VEHs

Power P_m (mW)	Frequency (Hz)	Mass M (g)	RMS Acceleration A_{rms} (m.s ⁻²)	Ratio $P_m/M A_{rms}^2$ (mW/g.m.s ⁻²)	Reference
27.14	2.8	171	0.748	0.039	(Jung et al. 2011)
0.118	3.7	56	0.25	0.104	(Kwon et al. 2013)
1.8	4.1	2400	0.02	6.761	presented device

586

List of Figures

587	1	Roberval bridge and view of its superstructure.	21
588	2	Sample of the time history acceleration response.	21
589	3	Mean power spectral density of the measured acceleration on the Roberval	
590		bridge.	22
591	4	Modal shape of the first bending mode of the bridge.	22
592	5	Synchronized measurements of the acceleration (top) and displacement (bot-	
593		tom).	23
594	6	Example of a pulse in the acceleration signal.	23
595	7	Histogram of the interarrival time	24
596	8	Girder beam of the Varese bridge.	24
597	9	Mean power spectral density of the measured acceleration on the Varese bridge.	25
598	10	Electromagnetic harvester.	25
599	11	Dimensions of the VEH (side and front views).	26
600	12	The two main components of the electromagnetic harvester.	26
601	13	Magnetic circuit (the gap in the z direction is exaggerated for better clarity).	
602		Magnets of the same color have the same magnetization.	27
603	14	Least squared identification of K and c_m	27
604	15	Map of B_z (in T) in the plane $(0, \mathbf{e}_x, \mathbf{e}_y)$	28
605	16	Example of a loop that maximizes K : The loop is parallel to \mathbf{e}_x within the	
606		domain \mathcal{R} shown in gray.	28
607	17	Optimal coil geometry (only a quarter of the coil is shown).	29
608	18	Cross-section of a compact packing of wires	29
609	19	Model geometry of the designed coil (only a quarter of the coil is shown). . .	30
610	20	Laboratory test of the harvester with an harmonic excitation.	31
611	21	Base excitation in the laboratory test.	32
612	22	Voltage measured across the load resistance during the laboratory test. . . .	32

613	23	Setup of the experimental device on the Roberval bridge.	33
614	24	Voltage measured across the load resistance during field testing.	33
615	25	Mean electrical output power vs oscillator frequency (Roberval bridge). . . .	34
616	26	Mean electrical output power vs oscillator frequency (Vareze bridge).	34
617	27	Pulse model.	35



FIG. 1. Roberval bridge and view of its superstructure.

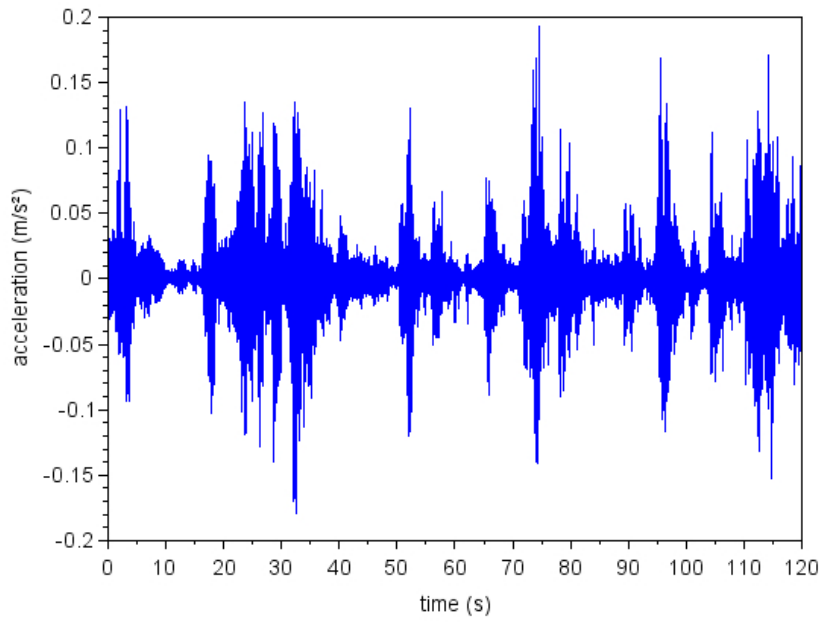


FIG. 2. Sample of the time history acceleration response.

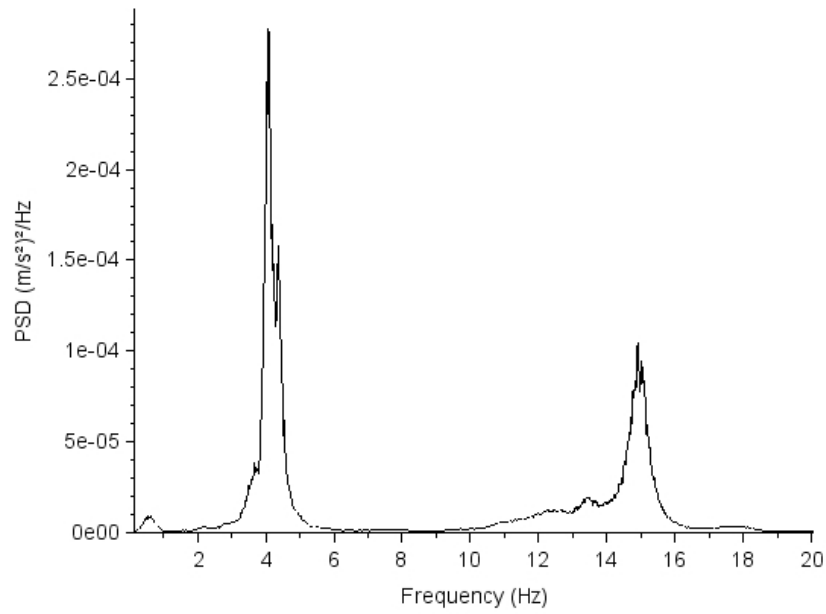


FIG. 3. Mean power spectral density of the measured acceleration on the Roberval bridge.

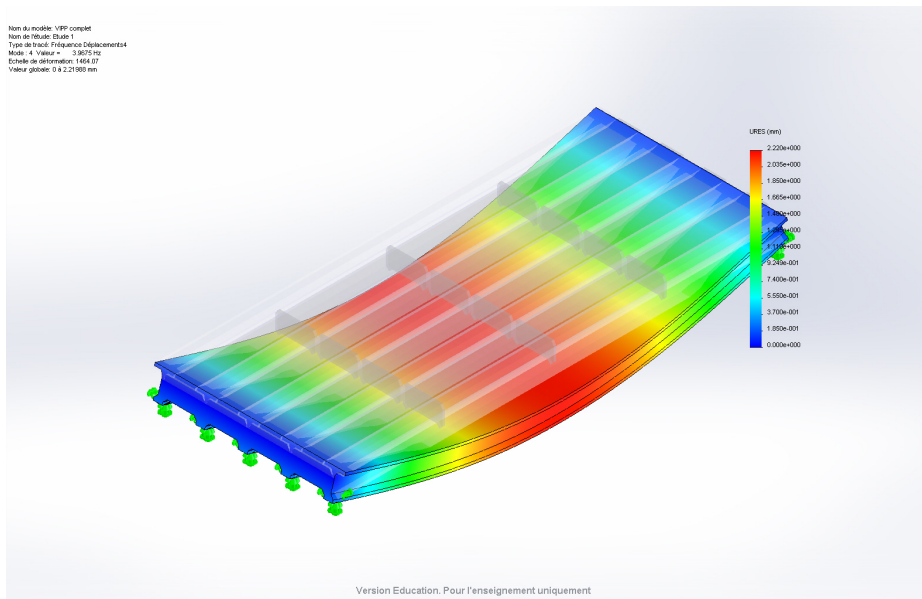


FIG. 4. Modal shape of the first bending mode of the bridge.

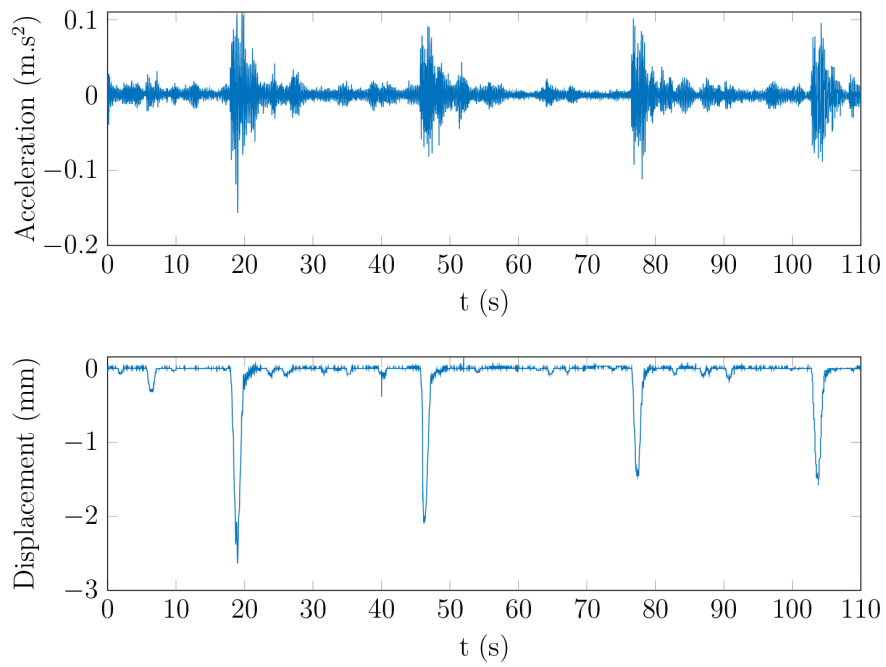


FIG. 5. Synchronized measurements of the acceleration (top) and displacement (bottom).



FIG. 6. Example of a pulse in the acceleration signal.

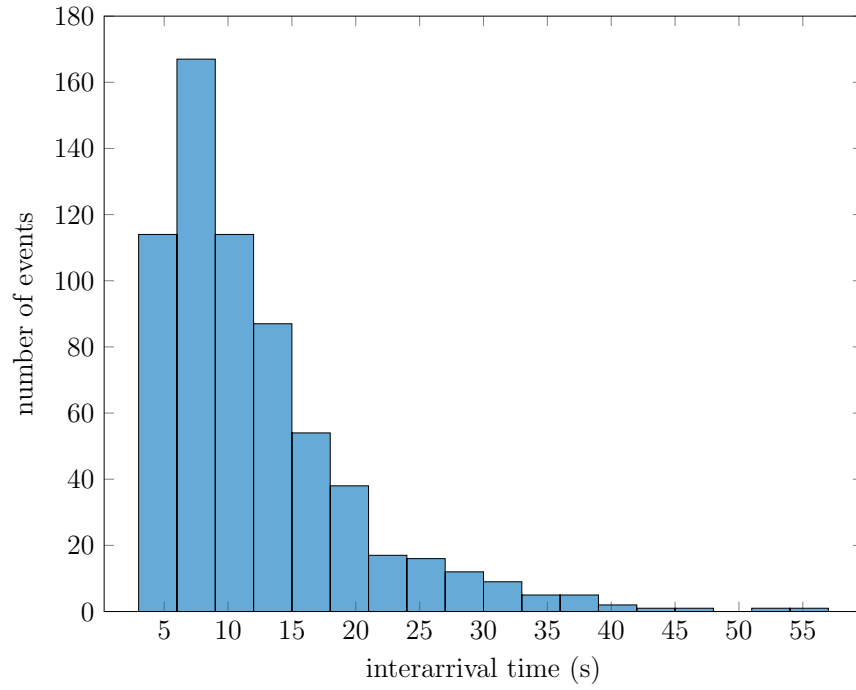


FIG. 7. Histogram of the interarrival time



FIG. 8. Girder beam of the Vazeze bridge.

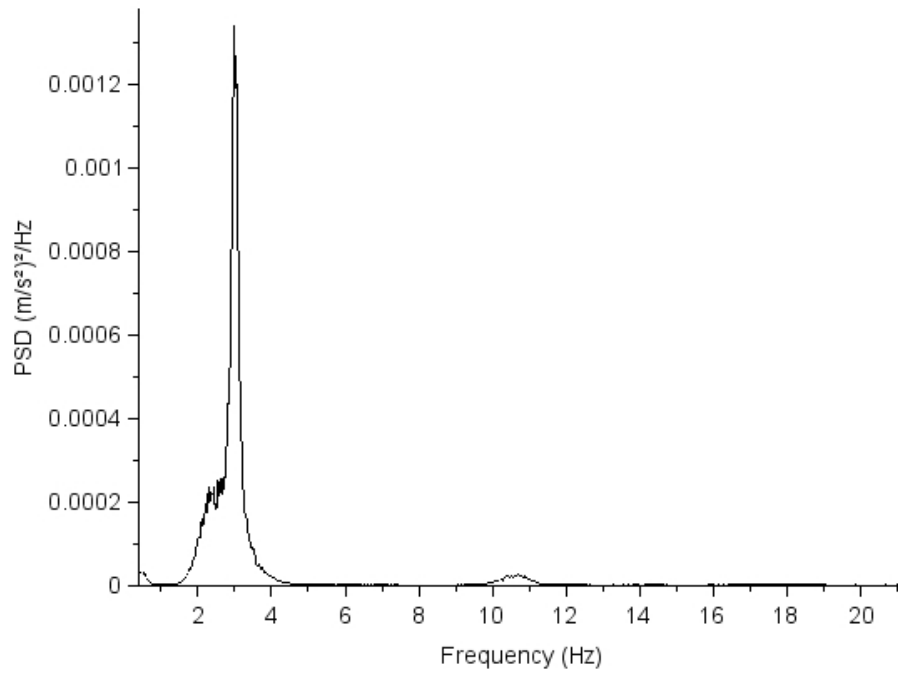


FIG. 9. Mean power spectral density of the measured acceleration on the Vazez bridge.

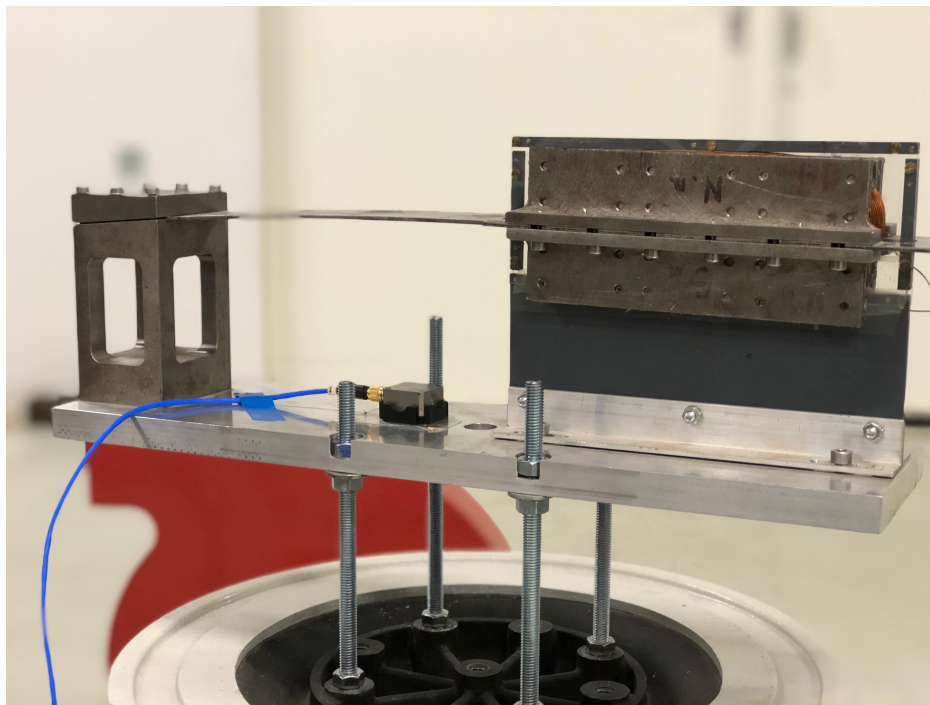


FIG. 10. Electromagnetic harvester.

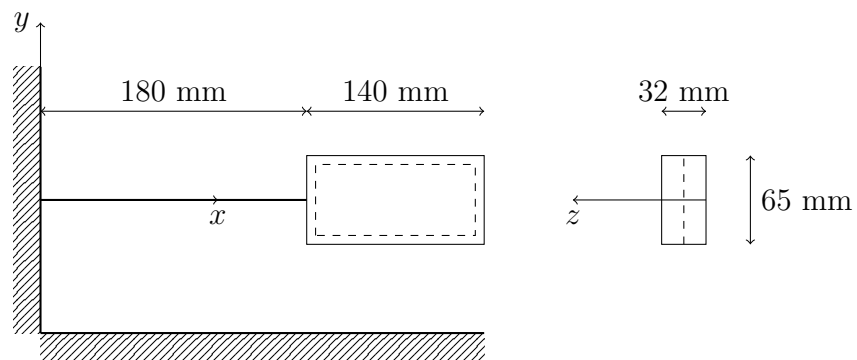


FIG. 11. Dimensions of the VEH (side and front views).

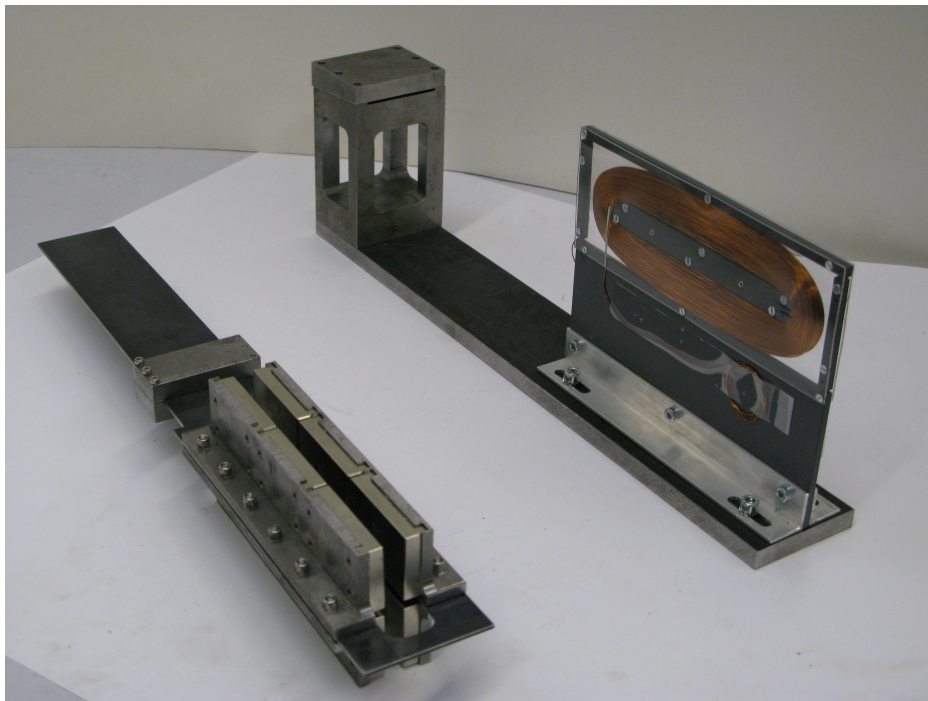


FIG. 12. The two main components of the electromagnetic harvester.

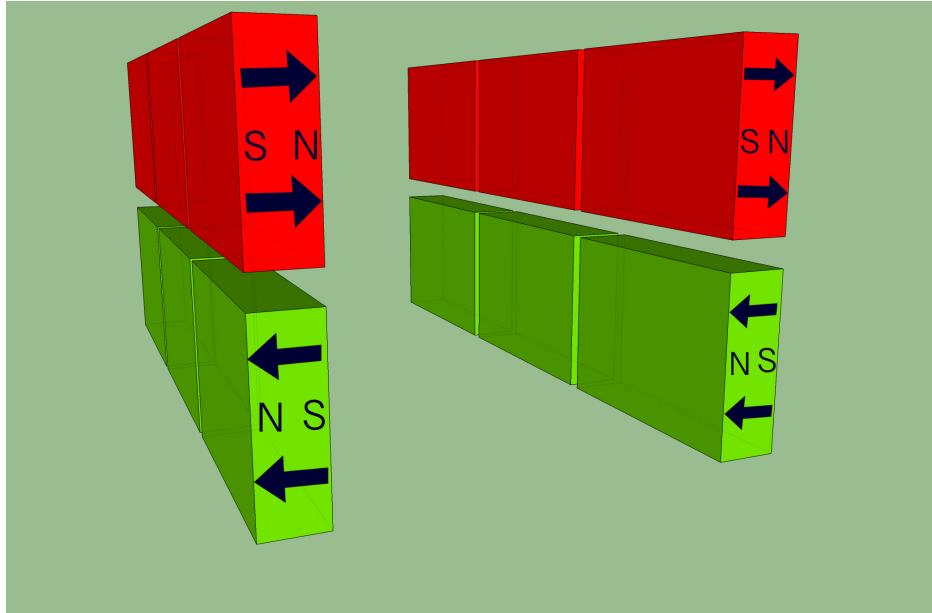


FIG. 13. Magnetic circuit (the gap in the z direction is exaggerated for better clarity). Magnets of the same color have the same magnetization.

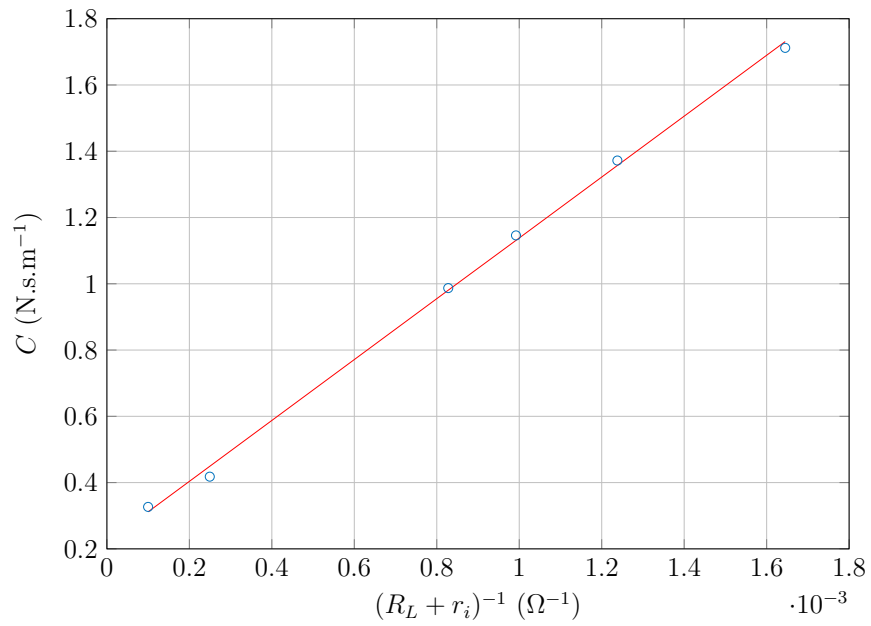


FIG. 14. Least squared identification of K and c_m .

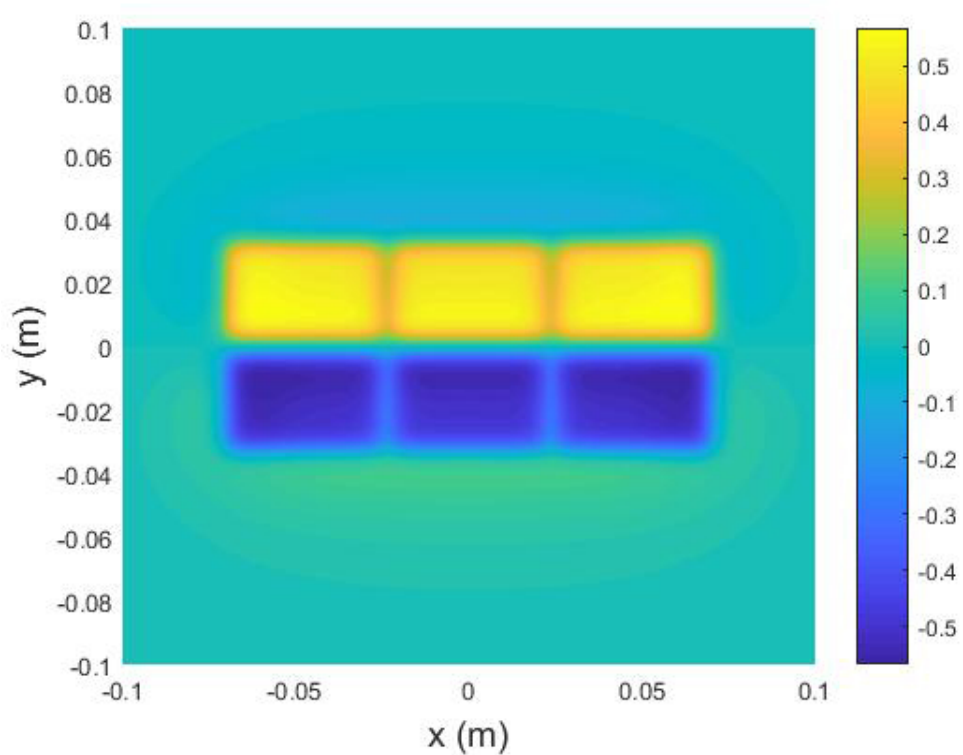


FIG. 15. Map of B_z (in T) in the plane $(0, e_x, e_y)$.

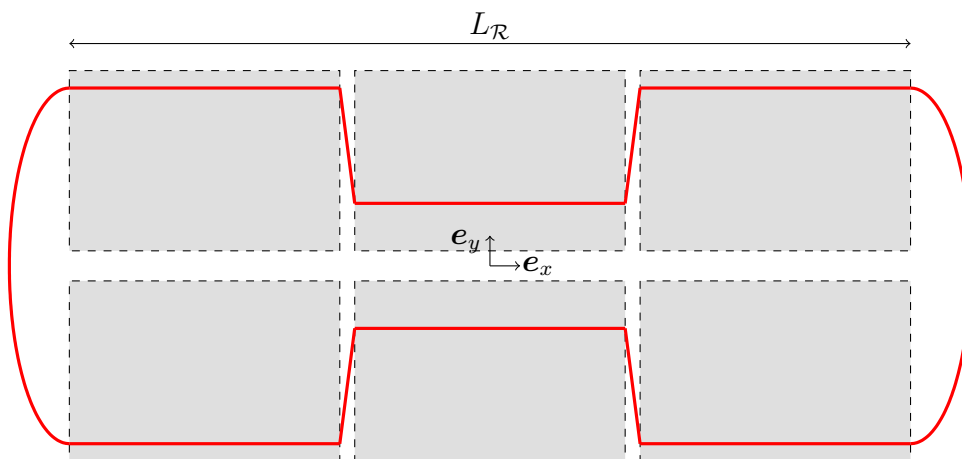


FIG. 16. Example of a loop that maximizes K : The loop is parallel to e_x within the domain \mathcal{R} shown in gray.

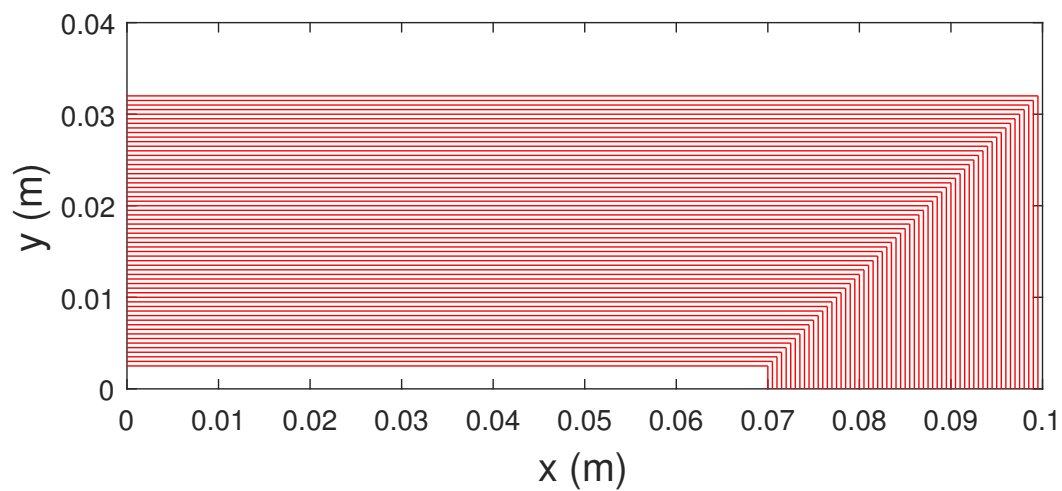


FIG. 17. Optimal coil geometry (only a quarter of the coil is shown).

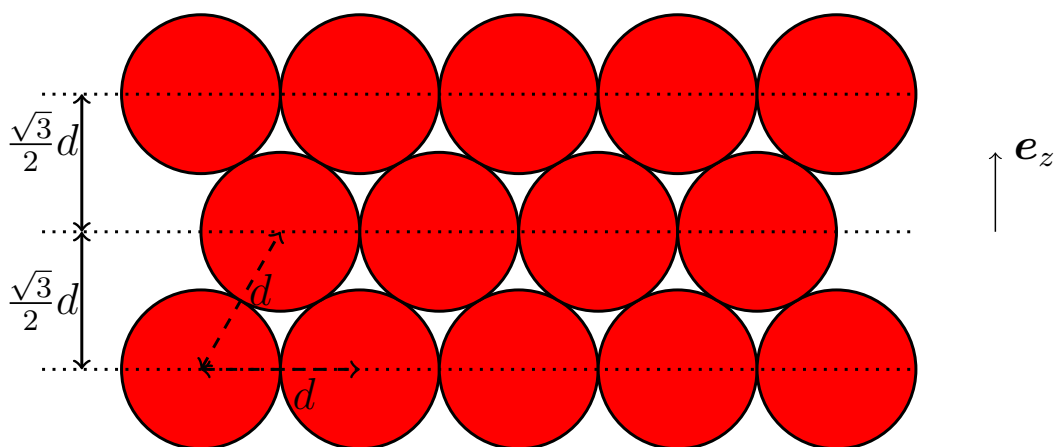


FIG. 18. Cross-section of a compact packing of wires

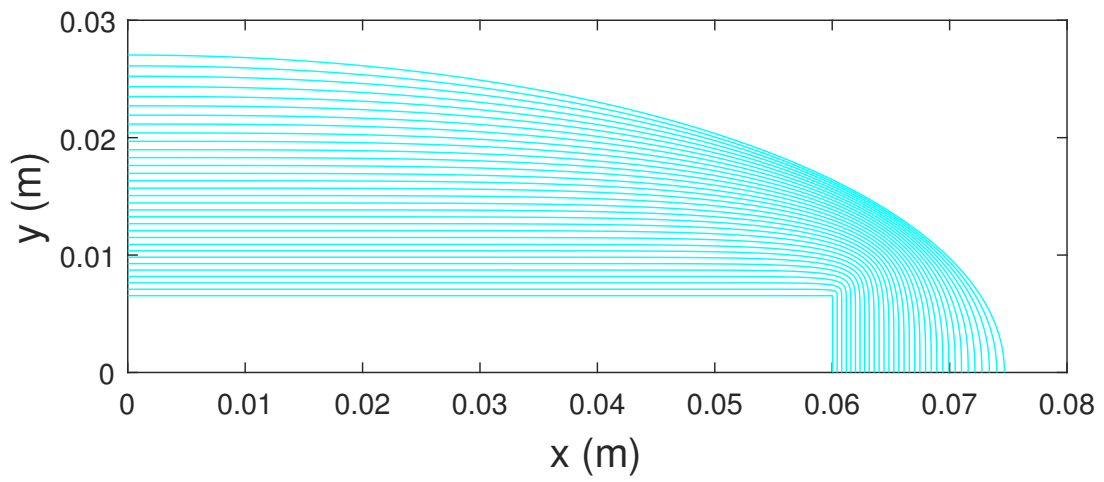


FIG. 19. Model geometry of the designed coil (only a quarter of the coil is shown).



FIG. 20. Laboratory test of the harvester with an harmonic excitation.

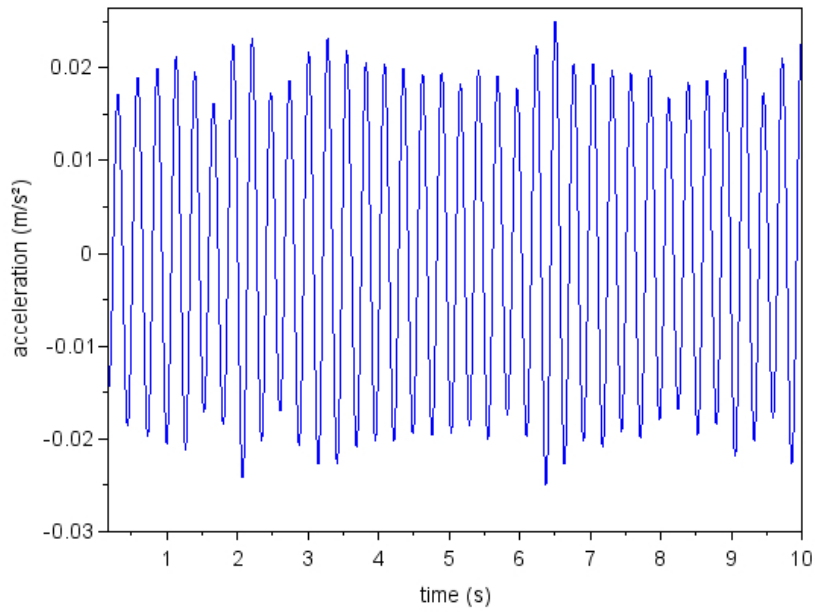


FIG. 21. Base excitation in the laboratory test.

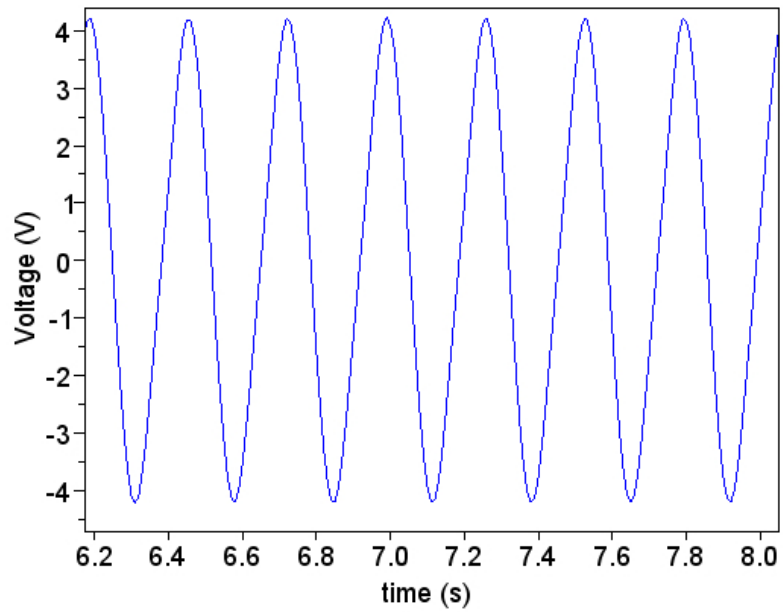


FIG. 22. Voltage measured across the load resistance during the laboratory test.

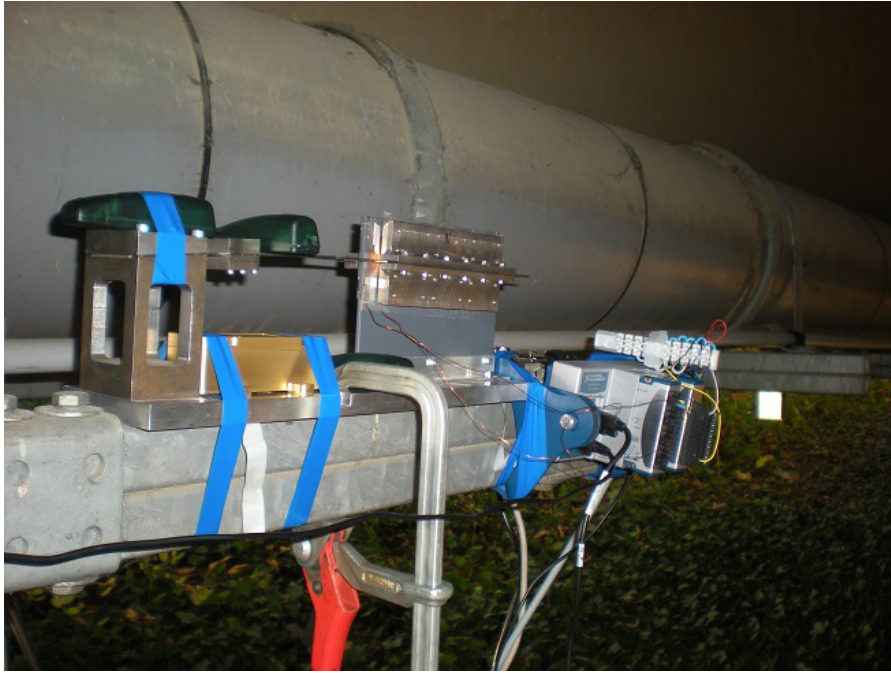


FIG. 23. Setup of the experimental device on the Roberval bridge.

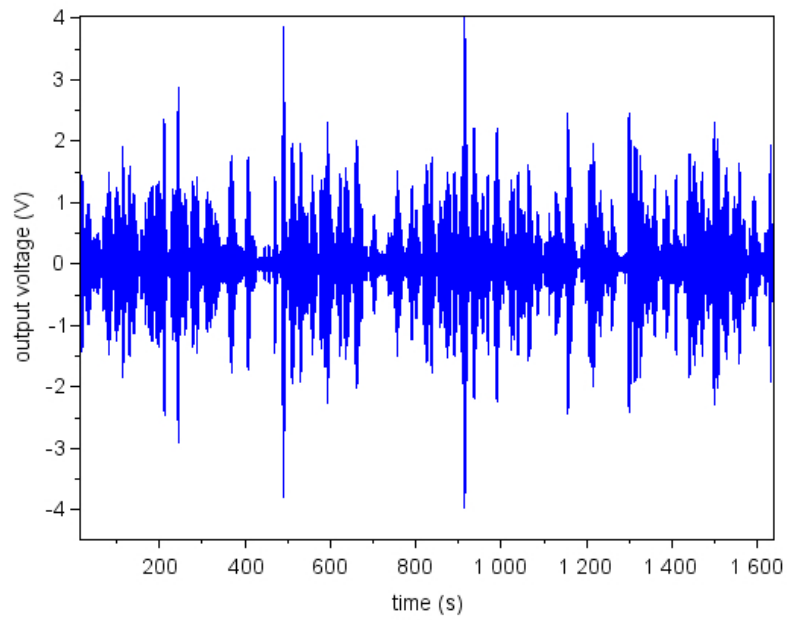


FIG. 24. Voltage measured across the load resistance during field testing.

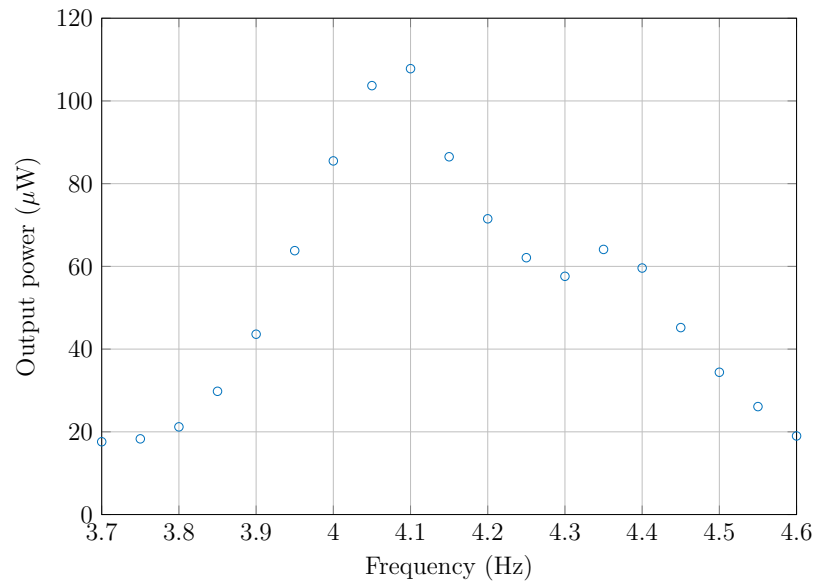


FIG. 25. Mean electrical output power vs oscillator frequency (Roberval bridge).

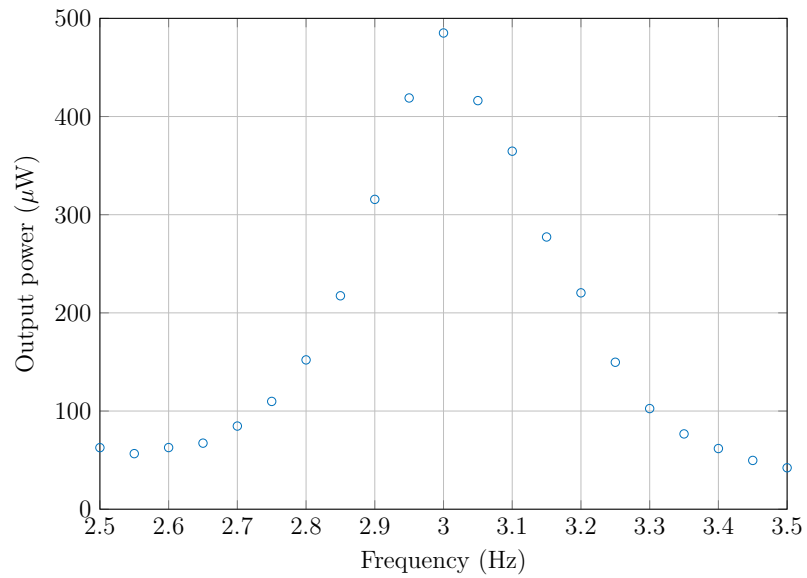


FIG. 26. Mean electrical output power vs oscillator frequency (Vazeze bridge).

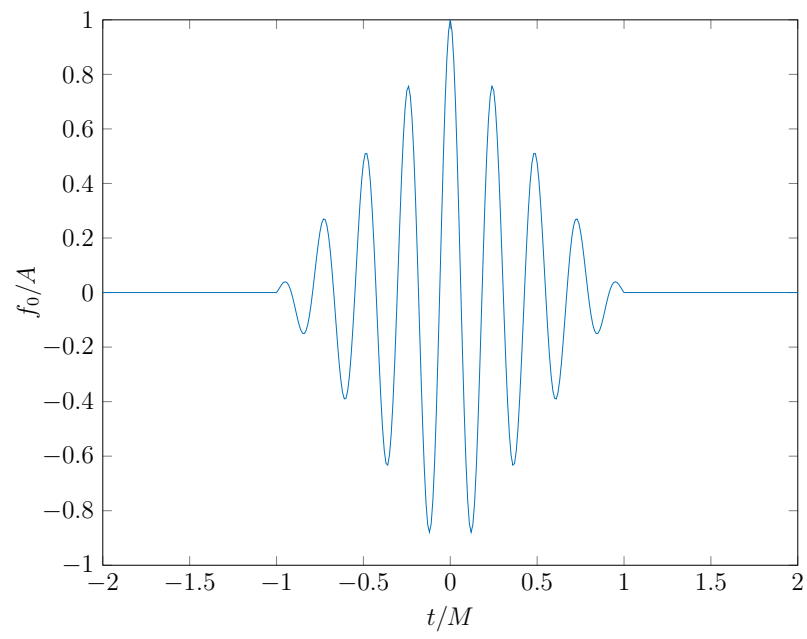


FIG. 27. Pulse model.